Anticancer potential of dendritic poly(aryl ether) substituted polypyridyl ligands based ruthenium(II)- coordination entities

Liju Raju, Sousa Javan Nikkhah, MosaChristas K, Matthias Vandichel, Rajkumar Eswaran

Supporting Information

Anticancer Potential of Dendritic Poly(aryl ether) Substituted Polypyridyl Ligands Based Ruthenium(II)- Coordination entities

Liju Raju[a], Sousa Javan Nikkhah[b], MosaChristas K[c], Matthias Vandichel[b] , and Eswaran Rajkumar[a*]

[a] Department of Chemistry, Madras Christian College (Autonomous), Affiliated to the University of Madras, Tambaram East, Chennai, Tamilnadu, India 600059.
[b] Department of Chemical Sciences and Bernal Institute, University of Limerick,Limerick V94 T9PX Republic of Ireland
[c] Department of Plant Biology and Biotechnology & Loyola Institute of Frontier Energy (LIFE), Loyola College (Autonomous), University of Madras, Chennai, India 600034
Email: rajjkumar@gmail.com

1. Synthesis and characterizations

1.1. Synthesis of Ruthenium(II)-cored metallodendrimers

The synthesis of **$[Ru(bpy)_2G_n\text{-bpy}]Cl_2$** complexes **RuG0, RuG1 and RuG2** involves the reaction of $[Ru(bpy)_2Cl_2.2H_2O]Cl_2$ and corresponding G_n-bpy ligands under inert atmosphere. The obtained residue was purified by column chromatography to obtain the complexes $[Ru(bpy)_2G0\text{-bpy}]Cl_2$ **(RuG0)**, $[Ru(bpy)_2G1\text{-bpy}]Cl_2$ **(RuG1)** and $[Ru(bpy)_2G2\text{-bpy}]Cl_2$ **(RuG2).**

1.1.2. Synthesis of 4,4'-bis[3'',5''-bis(2-(tert-butoxy)-2-oxoethoxy) benzyloxy]2,2'-bipyridine-bis(2,2'-bipyridine) Ruthenium (II) (RuG0)

The complex **RuG0** was obtained by the reaction of $[Ru(bpy)_2Cl_2]$ and G0-bpy in 1:1.05 ratio. The crude product was purified by column chromatography (SiO_2/dichloromethane: methanol 20:1 mixture); the product was obtained as red solid, Yield 70%. The FTIR spectrum of **RuG0** shown in **Figure S1** exhibit peaks at ν 2926 cm^{-1} (C-H, CH_3 stretching), ν 2931 cm^{-1} (C-H, CH_3 stretching), ν 1743(C=O, stretching), ν 1603 cm^{-1} (C=C, Ar), ν 1422 cm^{-1}(CH_2 bending), ν 1234 cm^{-1}(C-O, ether),), ν 1158 cm^{-1} (C-O aromatic ethers), ν 814.1 cm^{-1} (C-H bending Aromatic). The ^{1}H-NMR and ^{13}C-NMR spectrum of complex **RuG0** were measured in Acetone d_6 and is given in **Figure S2** and **S3** respectively. ^{1}H NMR (500 MHz, Acetone d6) δ 1.93(36H-CH_3), δ 4.43 (4H-CH_2), δ 4.55(4H- CH_2-O), δ 6.29(2H, Ar-H), δ 6.46(4H Ar-H), δ 7.90(2 H, Ar-H (bpy), δ 8.06(4 H Ar-H (bpy), δ 8.67 Ar-H (bpy). ^{13}C NMR (Acetone d6): δ 164.48, 159.70, 159.21, 138.38, 105.32, 101.38, 91.10, 81.02, 64.59, 65.45, 28.96. The ESI MS

spectrum of complex **RuG0** is shown in **Figure S4** , ESI MS $[M\text{-}2Cl_2]^{2+}$ 663.45 calculated (665.24), $[M\text{-}(Cl+C_6H_{11}O_2)]$ 680.48 calculated 680.18.

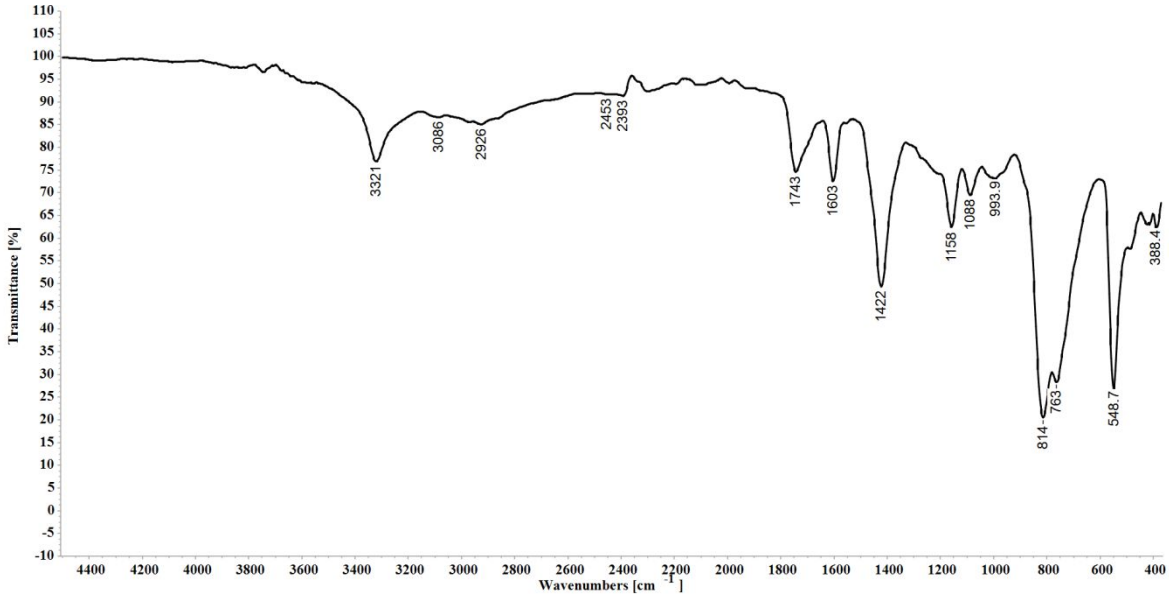

Figure S1. FTIR spectrum of **RuG0.**

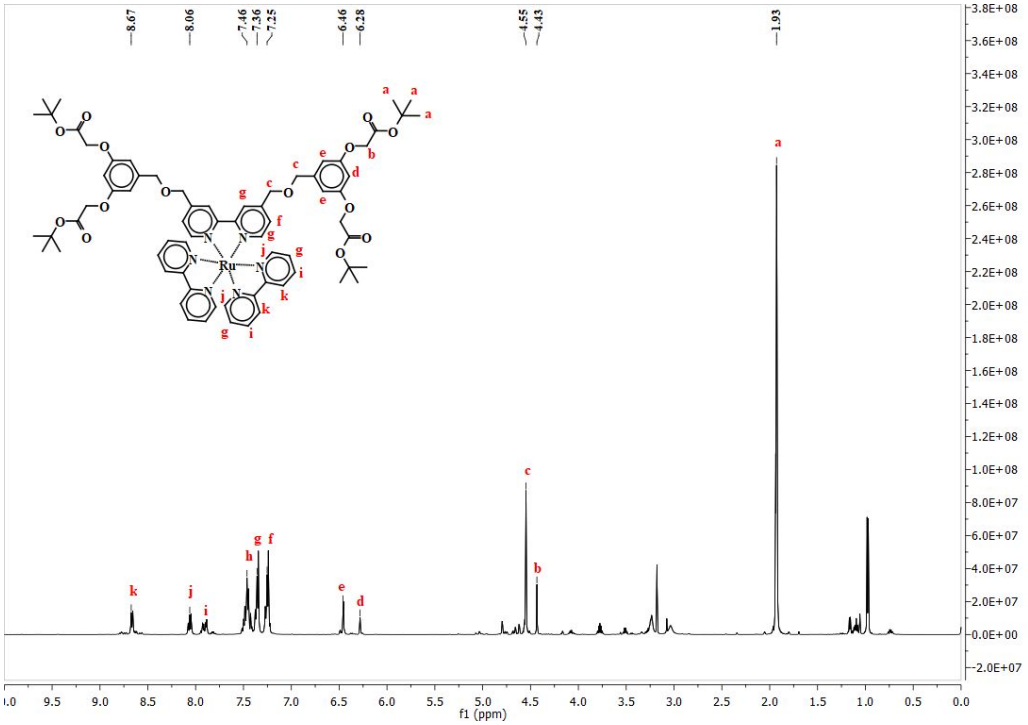

Figure S2. ^{1}H NMR spectrum of **RuG0** in deuterated acetone d_6

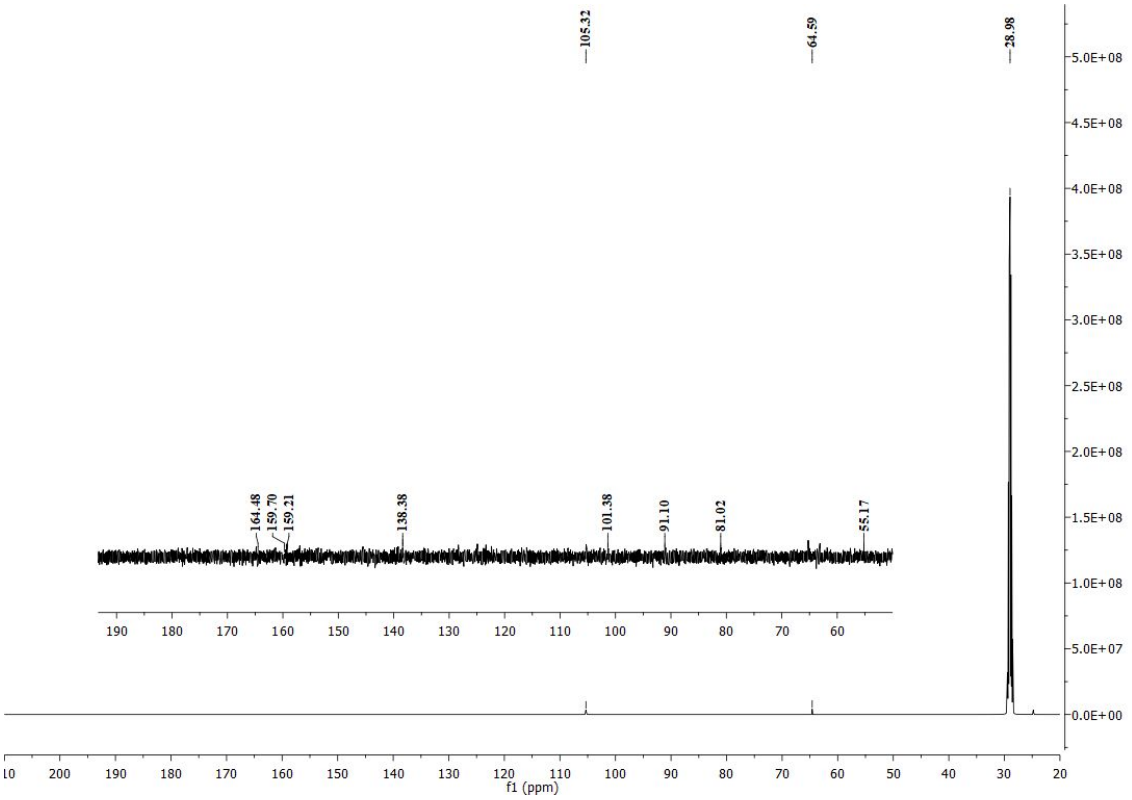

Figure S3. ^{13}C-NMR spectrum of **RuG0** in deuterated acetone d_6

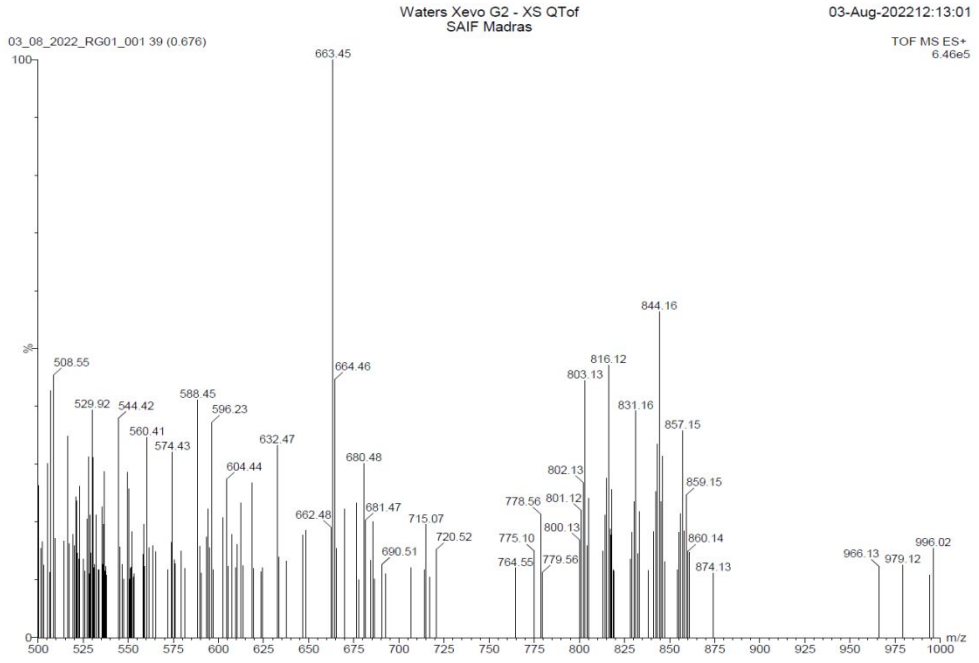

Figure S4. ESI MS spectrum of **RuG0.**

1.6.2. Synthesis of 4,4'-bis[3'',5''-bis[3''',5'''-bis(2-(tert-butoxy)-2-oxoethoxy) benzyloxy] benzyloxyl] 2,2'-bipyridine-bis(2,2'-bipyridine) Ruthenium (II) Chloride. (RuG1)

The complex **RuG1** was obtained by the reaction of $[Ru(bpy)_2Cl_2]$ and G1-bpy in 1:1.05 ratio. The crude product was purified by column chromatography(SiO_2/dichloromethane: methanol 20:1 mixture); the product was obtained as red oily liquid, Yield 72%. The FTIR spectrum of **RuG1** shown in **Figure S5** exhibit peaks at ν 2976 cm^{-1} (C-H, CH_3 stretching), ν 2926 cm^{-1} (C-H, CH_3 stretching), ν 1744(C=O, stretching), ν 1597 cm^{-1} (C=C, Ar), ν 1448 cm^{-1}(CH_2 bending), ν 1372 cm^{-1} (C-H, CH_3 stretching), ν 1230 cm^{-1}(C-O, ether),), ν 1140 cm^{-1} (C-O aromatic ethers), ν 834 cm^{-1} (C-H bending Aromatic). The ^{1}H-NMR and ^{13}C-NMR spectrum of complex **RuG1** were measured in Acetone d_6 and is given in **Figure S6** and **S7,** respectively. ^{1}H NMR (500 MHz, Acetone d_6) δ 1.33(72H, CH_3 s), δ 4.46-4.58(20H, -CH_2), δ 4.90 (4H, -CH_2 s), δ 6.29(6H Ar-H), δ 6.58 (12H, Ar-H), δ 7.22 (2H, Ar-H(bpy)) ,δ 7.43 (4H, Ar-H(bpy)), δ 7.89(4H, Ar-H(bpy)), δ 8.43(2H, Ar-H(bpy)), δ 8.77 (4H, Ar-H (bpy)). ^{13}C NMR (Acetone d6): δ 167.61, 159.94, 159.42, 145.25, 140.06, 106.41, 100.82, 81.32, 69.23, 65.45, 28.96. The ESI MS spectrum of complex **RuG1** is shown in **Figure S8.** ESI MS $[(M+CH_3)-(Cl_2+C_{44}H_{57}O_{14})]^{2+}$ 740.28 calculated 739.26, $[M-(Cl_2-8(C_5H_9O_2)]^{2+}$ 726.25 calculated 726.20 $[M-(Cl_2+C_{45}H_{59}O_{14})]^{2+}$ 725.76 calculated 725.76.

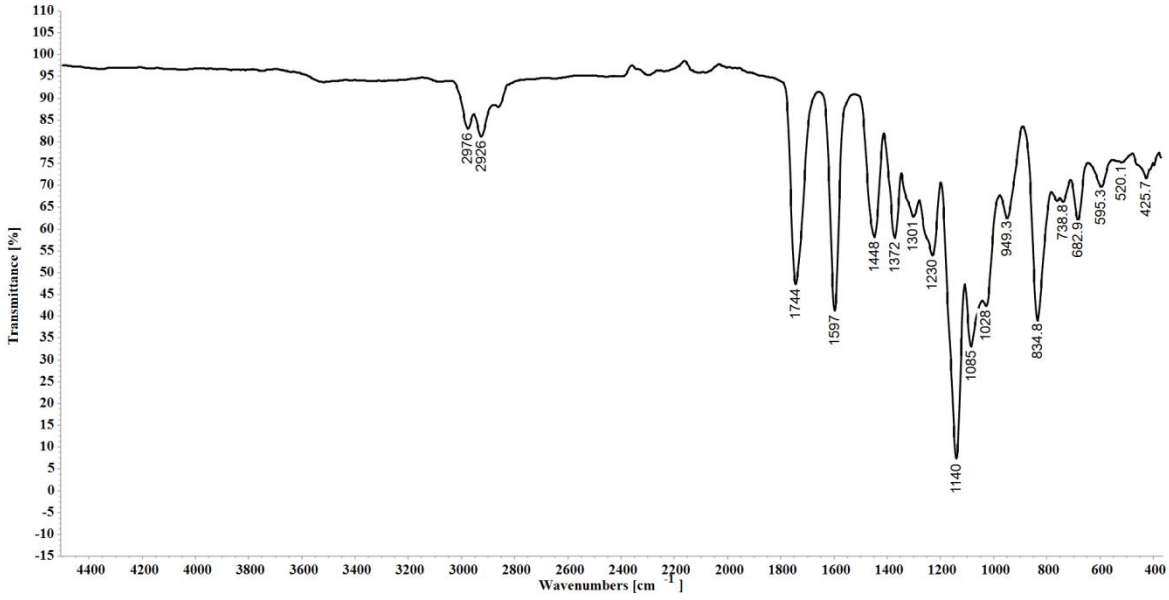

Figure S5. FTIR spectrum of **RuG1.**

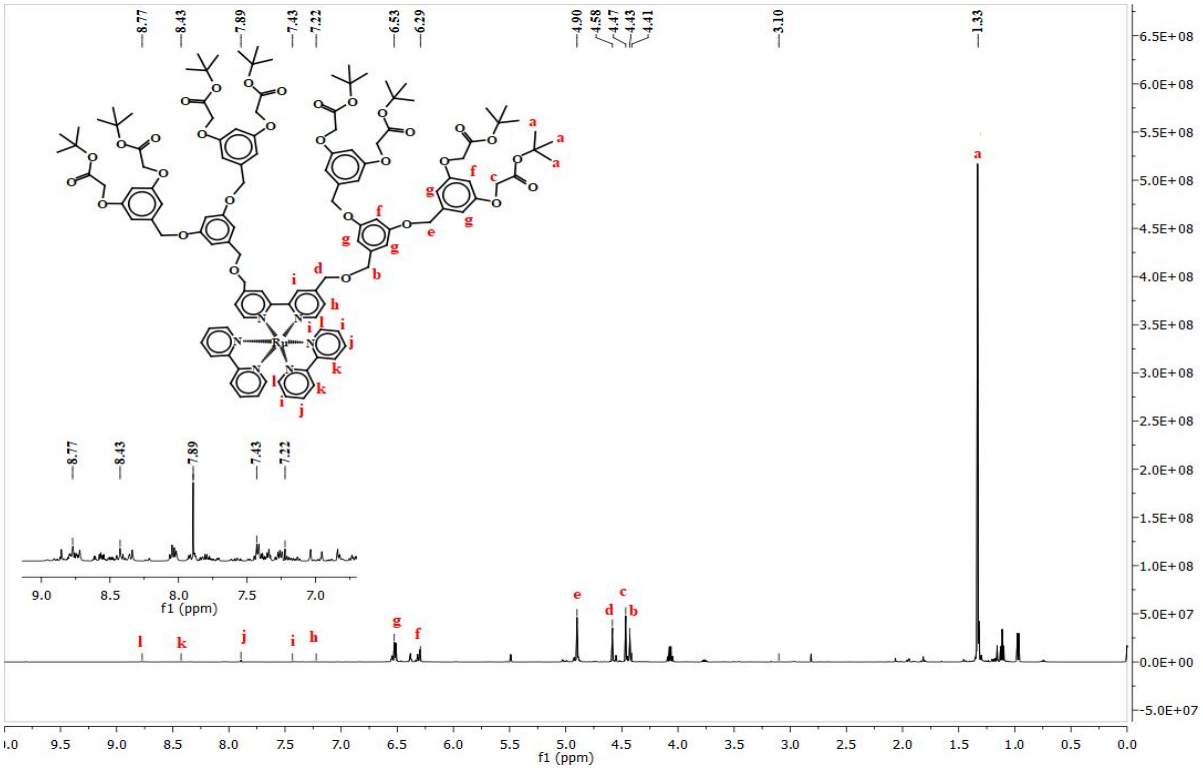

Figure S6. ^{1}H NMR spectrum of **RuG1** in deuterated acetone d_6.

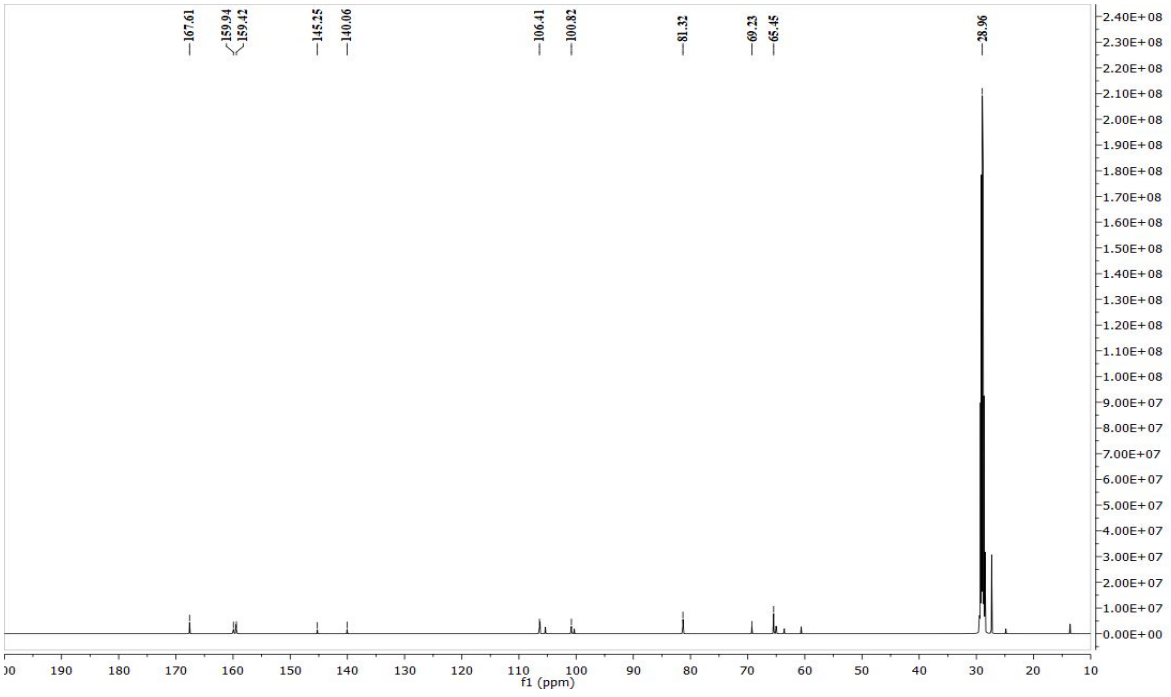

Figure S7. ^{13}C NMR spectrum of **RuG1** in deuterated acetone d_6.

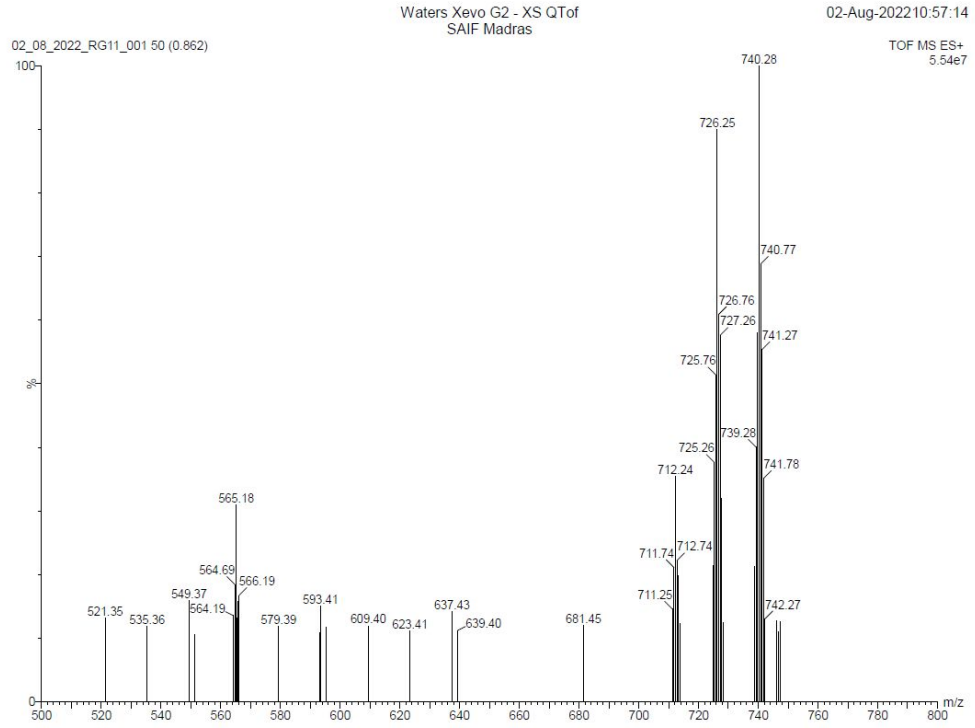

Figure S8. ESI MS spectrum of **RuG1.**

1.6.3. Synthesis of 4,4'-bis [3'',5''-bis [3''',5'''-bis [3'''',5''''-bis (2-(tert-butoxy)-2-oxoethoxy) benzyloxy] benzyloxy] benzyloxyl] 2,2'- bipyridine- bis(2,2'-bipyridine) Ruthenium (II) Chloride. (RuG2)

The complex **RuG2** was obtained by the reaction of $[Ru(bpy)_2Cl_2]$ and G2-bpy in 1:1.05 ratio. The crude product was purified by column chromatography (SiO_2/dichloromethane: methanol 20:1 mixture); the product was obtained as red oily liquid, Yield 68%. The FTIR spectrum of **RuG2** shown in **Figure S9** exhibit peaks at ν 2978 cm^{-1} (C-H, CH_3 stretching), ν 2931 cm^{-1} (C-H, CH_3 stretching), ν 1743(C=O, stretching), ν 1597 cm^{-1} (C=C, Ar), ν 1450 cm^{-1}(CH_2 bending), ν 1371 cm^{-1} (C-H, CH_3 stretching), ν 1213 cm^{-1}(C-O, ether),), ν 1139 cm^{-1} (C-O aromatic ethers), ν 834.8 cm^{-1} (C-H bending Aromatic). The ^{1}H-NMR and ^{13}C-NMR spectrum of Coordination entity **RuG2** were measured in Acetone d_6 and is given in **Figure S10 and S11** respectively. ^{1}H-NMR (500 MHz, Acetone d_6) δ 1.32 (144H, CH_3 s), δ 4.46 (32H, CH_2), δ 4.91 (8H CH_2), δ 4.92(24H), δ 6.30(14H), δ 6.53(28H Ar-H), δ 6.62 (2H Ar-H (bpy) δ 7.22 δ (2H, Ar-H (bpy), δ 7.45(4H Ar-H(bpy)), δ 7.90(4H Ar-H (bpy)), δ 8.04 (4H, Ar-H(bpy)), δ 8.73(4H Ar-H(bpy)). ^{13}C-NMR (Acetone d_6): δ 167.63, 166.23, 160.10, 159.51, 139.86, 106.39, 100.91, 81.35, 69.42, 65.45, 29.12. The ESI MS spectrum of Coordination entity **RuG2** is shown in **Figure S12.** ESI MS $[M-(Cl_2+C_{100}H_{131}O_{31})]^{2+}$ 1170.44 calculated 1169.435

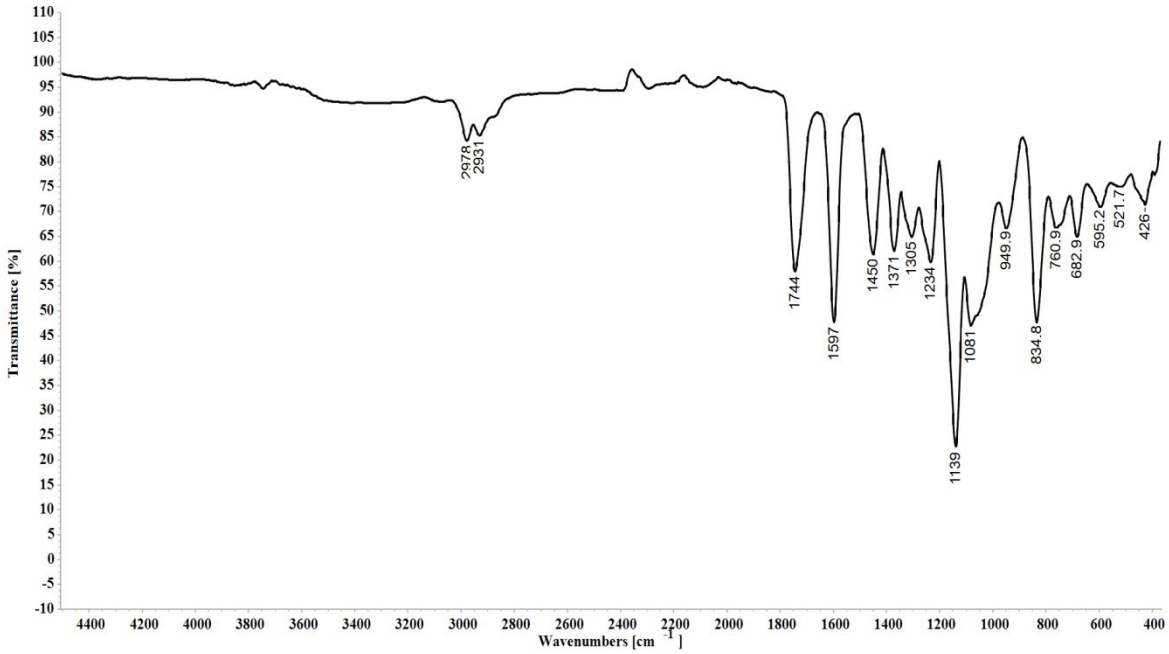

Figure S9. FTIR spectrum of **RuG2.**

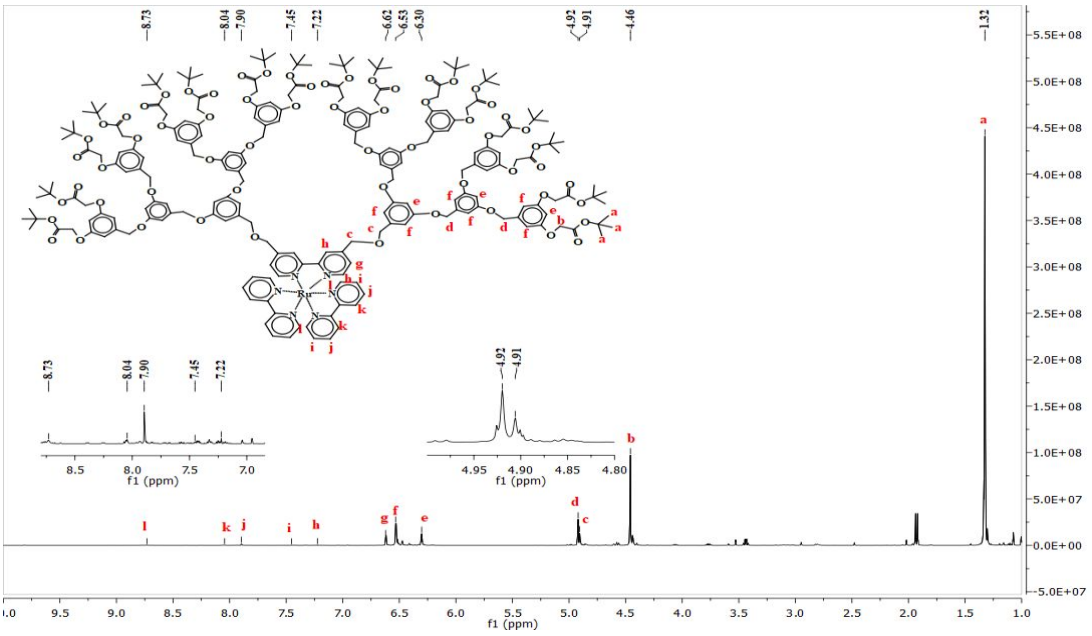

Figure S10. ^{1}H NMR spectrum of **RuG2** in deuterated acetone d_6.

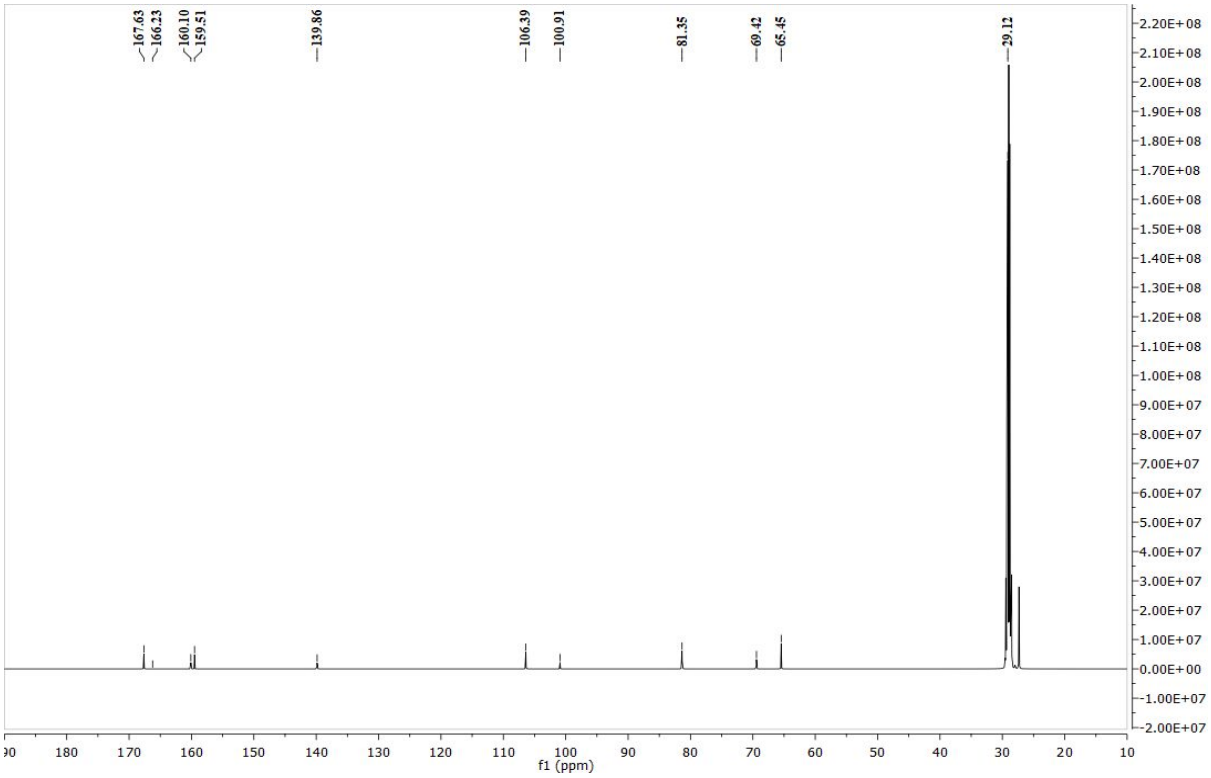

Figure S11. ^{13}C NMR spectrum of **RuG2** in deuterated acetone d_6.

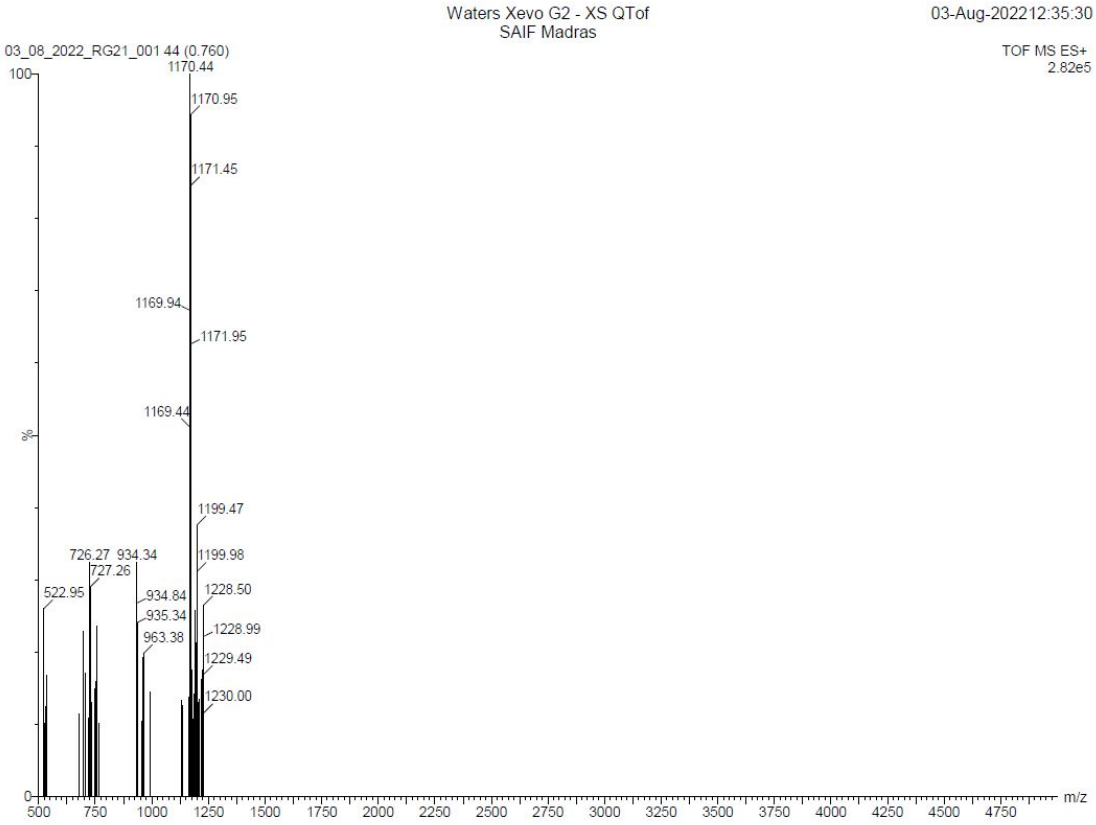

Figure S12. ESI MS spectrum of **RuG2.**

2 Molecular simulation studies

The initial coordinates of the Coordination entities were generated using Material Studio[1]. Bond lengths, bond angles, dihedral and improper angles, and vdW potential parameters were based on the Dreiding force field.[2,3] The atomic point charges were determined via the Charge equilibration (Qeq) method[4,5]. To ensure charge neutrality of the Ru^{2+}-Coordination entities, two chloride ions were added for each Ru. First, the Coordination entities were subjected to 2000 steps of steepest descent minimization, followed by 5000 steps of conjugate gradient minimization. Models of the optimized Coordination entities are presented in **Figure S13**.

Solvent molecules water and dimethyl sulfoxide (DMSO) were based on TIP3P[6] and Dreiding[2,3] parameters, respectively. The simulation trajectories were analysed in terms of the radius of gyration R_g, the solvent accessible surface area (SASA), and radial distribution function (RDF) $g_{ij}(r)$. The targeted Coordination entities were placed in the center of a cubic box, which was subsequently filled with solvent molecules. The initial models of the solvation boxes were built using Packmol[7,8] and Moltemplate[9] packages. First, we performed the steepest descent minimization of 5000 timesteps of 1 fs. After that, equilibration simulations were performed under the isothermal-isobaric ensemble (NPT), using the Berendsen barostat to maintain pressure isotropically at 1.0 bar (see Table S1 for more details). After the NPT equilibration, constant volume (NVT) equilibration simulations were performed (see **Table S1** for more details). Throughout all simulations, the temperature was maintained constant at 298.15 K using the Nose-Hoover thermostat.[10] Further simulation details, including box size, number of molecules, concentration, and simulation time, are presented in the **Table S1.**

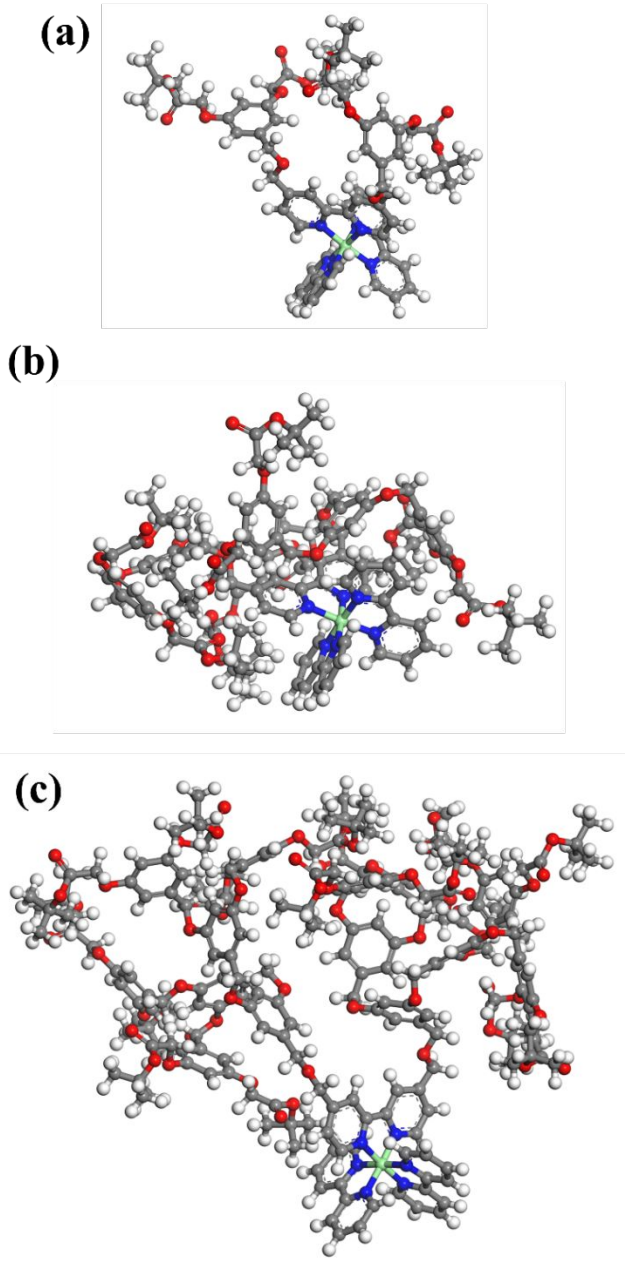

Figure S13. Optimized molecular structures of (a) RuG0, (b) RuG1, and (c) RuG2, were taken as initial configurations for the molecular dynamics (MD) simulations. Carbon, oxygen, nitrogen, hydrogen, and Ruthenium atoms are represented in grey, red, blue, white, and green balls, respectively.

Table S1. Models and simulation details of ruthenium (II) Coordination entities of G0-bpy, G1-bpy, and G2-bpy ligands

Coordination entities	Initial simulation box size (Å×Å×Å)	Number of polymer molecule	Solvent	Number of solvent molecules	Conc. (mg/ml)	Simulation time (NPT) (ns)	Simulation box size after the NPT simulation (Å³)	Final conc. (mg/ml)	Simulation time (NVT) (ns)
RuG0	50×50×50	1	Water	4181	17.28	15	173927.99	12.42	70
	50×50×50	1	DMSO	1050	17.68	15	148035.89	14.93	70
RuG1	50×50×50	1	Water	4181	30.24	15	153474.10	24.62	70
	50×50×50	1	DMSO	1050	30.24	15	178834.18	21.13	70
RuG2	60×60×60	1	Water	7200	32.03	15	239714.52	24.63	70
	60×60×60	1	DMSO	1810	32.03	15	304821.22	21.13	70

2.1. Autocorrelation function of radius of gyration

After the MD simulations, we calculated the autocorrelation function of the radius of gyration ($C_{R_g}(t)$) for the Coordination entities using the following expression to evaluate if the equilibrium state was achieved:

$$C_{R_g}(t) = \frac{< (R_g^2(t) - < R_g^2 >)(R_g^2(0) - < R_g^2 >) >}{< R_g^4 > - < R_g^2 >^2} \quad (1)$$

The $C_{R_g}(t)$ graphs for all simulated systems are presented in **Figure S14**. According to **Figure S14**, the $C_{R_g}(t)$ curves fluctuate around zero, indicating that the simulation times were long enough to give well-equilibrated conformations. Generally, for polymers, $C_{R_g}(t)$ is strongly affected by the ability of the chains to deform. Even in the equilibrated state, chain deformation and rotation can occur due to the flexibility of the chains, such that the chains can experience $R_g^2(t)$ higher or lower than $< R_g^2 >$, which causes positive and negative $C_{R_g}(t)$ values, respectively.

We also determined the Coordination entities' relaxation times (τ_r), defined as the time when $C_{R_g}(t)=1/e$ (where e is Euler's number = **2.71828**). τ_r results are shown as inset tables in **Figure S14**. According to the relaxation time, the simulation times were long enough to give equilibrated configurations for modeling the structural and dynamical properties of the Coordination entities.

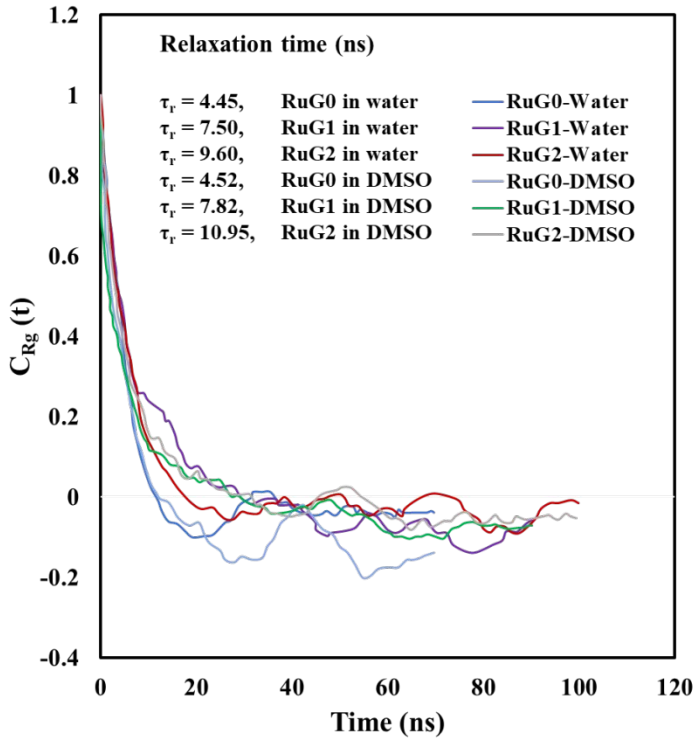

Figure S14. Autocorrelation function of the radius of gyration as a function of time $C_{Rg}(t)$ for RuG0, RuG1, and RuG2 Coordination entities in water and DMSO. The values in the graph are the calculated relaxation times (τ_r).

2.2. Simulation post-processing and trajectory analysis method

The simulation trajectories were analyzed to determine the radius of gyration R_g, solvent accessible surface area (SASA), and radial distribution function $g_{ij}(r)$.

2.2.1. Radius of gyration. Dendrimer size can be quantitatively estimated by the mean-square radius of gyration (R_g), computed as[11]

$$R_g = \sqrt{\langle R_g^2 \rangle} = \frac{1}{M} < \sum_{i=1}^{N} [\boldsymbol{m_i} | \boldsymbol{r_i} - \boldsymbol{R}|^2] > \quad (2)$$

where N is the number of dendrimer atoms, M is the total dendrimer mass, $\boldsymbol{m_i}$ and $\boldsymbol{r_i}$ are, respectively, the mass and the coordinate vector of the i^{th} atom, $\boldsymbol{R}$ is the coordinate vector of the center of mass, and the angle brackets stand for time averaging. The last 7 ns of the simulation trajectories were considered for averaging.

2.2.2. Solvent accessible surface area (SASA). The use of dendritic polymers as a guest-host system for drug delivery and other technological applications relies on the available surface area of dendrimers. In order to evaluate the area available for Coordination entity interactions

with water and other molecules, we performed calculations of the solvent accessible surface area (SASA) of the dendrimers in both water and DMSO. The average SASA and its standard deviation were calculated using the last 7 ns of the simulations, to find the extent of dendrimer surface area exposure to the solvent environment.

2.2.3. Radial Distribution Function. The radial distribution function $g_{ij}(r)$ was calculated from a distance histogram constructed by counting the number of atoms located in spherical shells of radius r and thickness Δr.

$$g_{ij}(r) = \left(4\pi r^2 \rho\, \Delta r\right)^{-1} < N_{ij}(r;\Delta r) > \qquad (3)$$

where ρ is the average number density, Δr is the bin width of the distance histogram, N_{ij} is the number of i sites around j sites at a distance between r - $\Delta r/2$ and r + $\Delta r/2$, and the angle brackets denote trajectory averaging that occurred over the last 10 ns of the simulations.

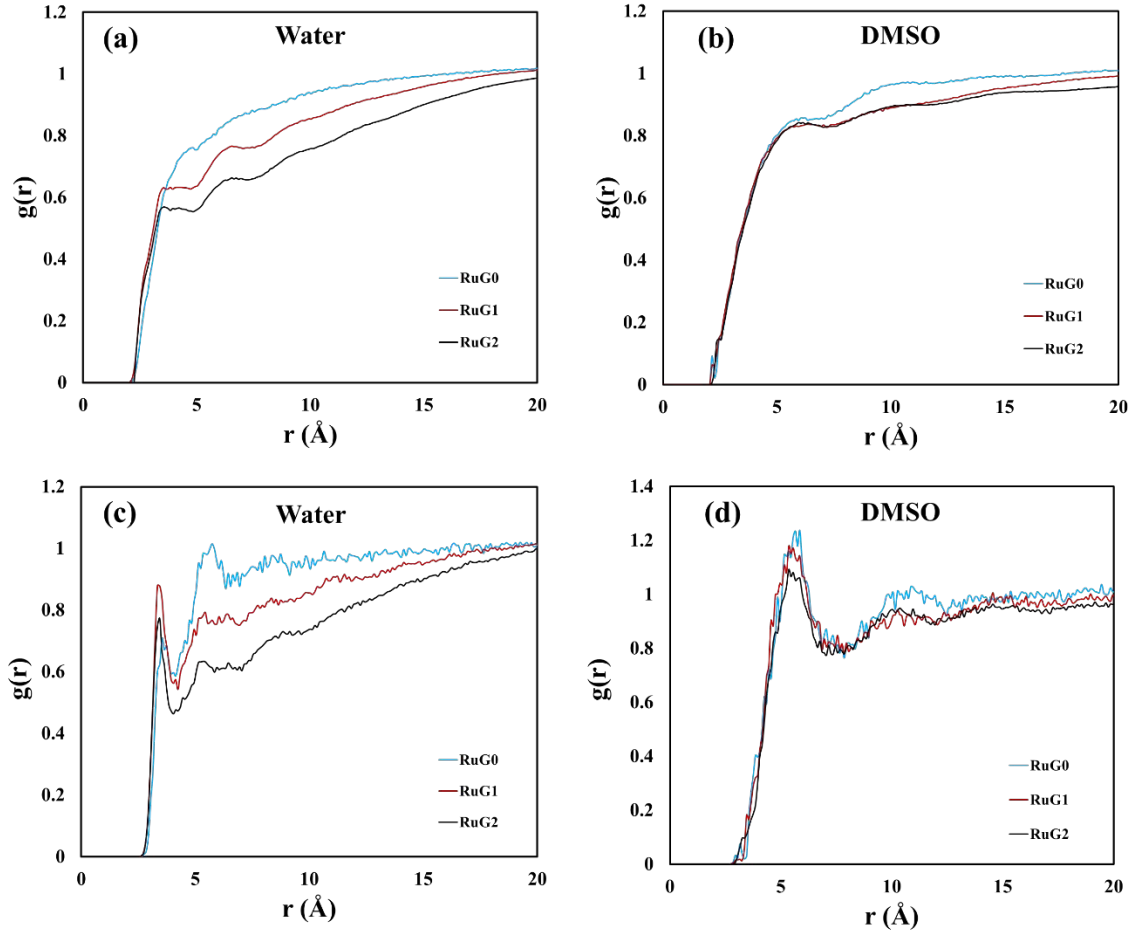

Figure S15. Radial distribution function between (a) the Coordination entities and water molecules, (b) the Coordination entities and DMSO molecules, (c) the oxygen atoms of the coordination entities and water molecules, and (d) the oxygen atoms of the coordination entities and DMSO molecules. g(r) data analysis is based on the last 10 ns of the simulations.

2.3 Cytotoxicity studies by MTT assay

A549 lung adenocarcinoma cell line, MDA MB 231 human breast epithelial adenocarcinoma cell lines, HepG2 liver cancer cell, and normal kidney epithelial cell line Vero were obtained from the National Centre for Cell Sciences (NCCS), Pune, India. In the present study, the normal Vero epithelial cell line serves as a reference for evaluating the relative cytotoxicity[12,13]. Cells were maintained in the logarithmic growth phase of Dulbecco's modified Eagle medium (DMEM) complemented by 10% (v/v) heat-inactivated fetal bovine serum (FBS), 100 U/ml penicillin, 100 μg/ml streptomycin. They were maintained at 37°C with 5% CO_2 in a 95% humidified air incubator.

The cells were seeded in 96-well microplates (1×10^5 cells per well) and incubated at 37°C for 48 h in 5% CO_2 incubator and allowed to grow to 70–80% confluence. The medium was then replaced, and the cells were treated with different concentrations (10, 20, 40, 80, and 160 μg/ml) of Ru(II) coordination entities **RuG0, RuG1, and RuG2** and cisplatin as a control drug[14] and incubated for 24 h. After 24 h, the morphological variations of DMSO blank (control), cisplatin, and Ru(II) coordination entities treated cells were observed under an inverted microscope (Magnus INVI; 40× magnification) and were photographed. The cells were then washed with phosphate buffer saline (PBS, pH 7.4), and 20 μl of MTT solution (5 mg/ml in PBS) was added to each well, and the plates were then kept at 37°C in the dark for 3 h. Formazan crystals were dissolved in 100 μl DMSO, and their absorbance was monitored at 570 nm. In the MTT assay, formazan accumulation directly represents mitochondrial activity in live cells, which is an indirect indicator of cell viability.

The percentage of cell viability was calculated using the following equation

$$\text{Cell viability \%} = [\text{Absorbance of the sample}/\text{Absorbance of the control}] \times 100 \quad (1)$$

The graph was plotted between cell viability (%) and sample concentration. The IC_{50} concentration at which 50% of cell growth processes are inhibited was calculated using GraphPad Prism version 8 software.

2.4 Apoptotic morphological detection by Acridine orange/ Ethidium bromide AO/EB dual staining

Fluorescence microscopic study of A549 lung adenocarcinoma cell line, MDA MB 231 human breast epithelial adenocarcinoma cell lines, and HepG2 liver cancer cell stained with AO and EB was carried out to understand the morphological changes of the cells upon treatment with

the prepared Ru(II) coordination entities[15]. The cells were cultured in a 6-well plate (1×10^5 cells per well) plates and incubated at 37 °C for 48 h. Then coordination entities **RuG0, RuG1,** and **RuG2,** at their IC_{50} concentrations, were incubated with the A549, MDA MB 231, and HepG2 cells. After incubation, AO (100 μg/mL) and EB (100 μg/mL) were added to each well for 5 min then the stained cells were examined via a fluorescence microscope (Invitrogen EVOS FL Cell Imaging; 40× magnification) for any morphological changes.

2.5 Nuclear morphology analysis by DAPI staining

The nuclear morphology changes (condensed chromatin and fragmented nuclei) in the **RuG0, RuG1,** and **RuG2** treated A549; MDA MB 231 and HepG2 cells were examined with DAPI (4'-6'-diamidino-2-phenylindole) staining assay[16]. In a 6-well plate, 1×10^5 cells per well were cultured and exposed with IC_{50} concentration of Ru(II) coordination entities **RuG0, RuG1,** and **RuG2** for 24 h. Upon incubation, the cells were washed with PBS and fixed with 3% paraformaldehyde (50 μl) for 10 min and then permeabilized with 0.2% Triton X-100 (50 μl) for 10 min at room temperature. The cells were then stained with 10 μl of DAPI stain (0.5 μg/ml), kept for 5 min, and visualized under the fluorescence microscope.

2.6 Cell death analysis by propidium iodide (PI) staining

The cultured A549, MDA MB 231, and HepG2 cells in a 6-well plate (1×10^5 cells per well) were treated with IC_{50} concentration of the synthesized Ru(II) coordination entities and incubated for 24 h[17]. After 24 h, the cells were washed with PBS fixed in methanol: acetic acid (3:1, v/v) for 10 min and stained with 10 μL of PI stain (50 μg/ml) for 20 min. Then the apoptotic nucleus of cells was viewed under the fluorescence microscope.

2.7 Reactive Oxygen Species (ROS) Assay

The intercellular reactive oxygen species (ROS) generation in RuG0, RuG1, and RuG2 treated A549, MDA MB 231, and HepG2 cells was determined by oxidative conversion of non-fluorescent cell-permeable dichlorodihydrofluorescein diacetate into fluorescent 2',7'-dichlorofluorescein dye[18,19]. For the ROS assay, the A549, MDA MB 231 and HepG2 cells were treated with IC_{50} concentration of Ru(II) coordination entities (**RuG0, RuG1,** and **RuG2**) in a 6-well plate (1×10^5 cells per well) and incubated for 24 h. Subsequently, the treated cells were stained with 1 μl of 40μM Dichlorodihydrofluorescein diacetate and kept for 20 min in dark condition. The formation of 2',7'-dichlorofluorescein dye inside the cells was determined using a fluorescence microscope.

2.8 Assessment of mitochondrial membrane potential (Δψm)

The mitochondrial membrane potential (Δψm) of A549, MDA MB 231, and HepG2 cells was assessed using the cationic fluorescent dye Rhodamine 123[20]. The cells were cultured in a 6-well plate 1x10^5 cells/well. Following treatment with IC_{50} concentration of Ru(II) coordination entities (**RuG0, RuG1,** and **RuG2**), the culture medium was carefully removed, and cells were washed twice with PBS. The cells were subsequently stained with 2 μM Rhodamine 123 for 20 min at 37˚C in the dark. Cells were examined under a fluorescence microscope at 40× magnification.

2.9 Apoptotic DNA ladder assay.

The DNA ladder assay, used to detect apoptosis, was performed with a slight modification. Initially, HepG2 cells were cultured overnight in 25 cm^2 flasks and then exposed to a concentration IC_{50} of **RuG0, RuG1, RuG2** for 24 hours. Subsequently, the cells were gently scraped and collected through centrifugation. To initiate the assay, the harvested cells were suspended in 0.5 ml of lysis buffer containing 10 mM Tris-HCl, 0.5 mM EDTA (pH 8.0), 2% SDS, and 1 mM NaCl. The cell suspension was then incubated at 37°C for 15 minutes. Proteinase K (20 mg/ml) was added to the mixture to purify the DNA and denature the proteins, followed by incubation at 50°C for 45 minutes. Next, DNA extraction was carried out using an equal volume of phenol:chloroform:isoamyl alcohol (25:24:1) solution. The extracted DNA was then treated with 3 M sodium acetate (100 μl) for precipitation, and the DNA pellet was washed with ice-cold 70% ethanol (200 μl). To visualize the DNA fragments, electrophoresis was performed on 1.5% agarose gels containing 0.1 μg/ml ethidium bromide. Finally, an image of the DNA bands was captured using a gel documentation system.

2.10. Molecular Docking analysis with DNA

Molecular docking studies of the coordination entities **RuG0, RuG1,** and **RuG2** and cisplatin were performed using Autodock 1.5.6 software. Two types of DNAs were used for docking purposes: B-DNA (PDB ID: 1BNA) was used for the groove binding possibility, and 6 bp DNA (PDB ID: 1Z3F) was used for evaluation of the intercalation possibility, the X-ray crystal structure were retrieved as a PDB file from the Protein Data Bank[21]. The structures of synthesized dendritic coordination entities and cisplatin were pre-optimized, all water and heteromolecular were removed, Kollman charges were added, and the PDB files of both the coordination entities and macromolecule were converted to the standard PDBQT format applying Auto Dock Tools 1.5.6[22]. The covered volume of the grid box was prepared to occupy the entire DNA molecule with 40 × 40 × 80 and 50 × 50 × 80 points along the $X \times Y \times Z$ direction with a 0.5 Å grid spacing for 1BNA and 1Z3F, respectively. The lowest energy conformations

were considered as the best docked poses. The 3D docked protein–Ru(II) coordination entity poses were visualized using the Schröodinger Maestro *V 2022-2* software program[23].

3. Fluorescence imaging studies

3.1. Apoptotic morphological detection by Acridine orange/ Ethidium bromide AO/EB dual staining

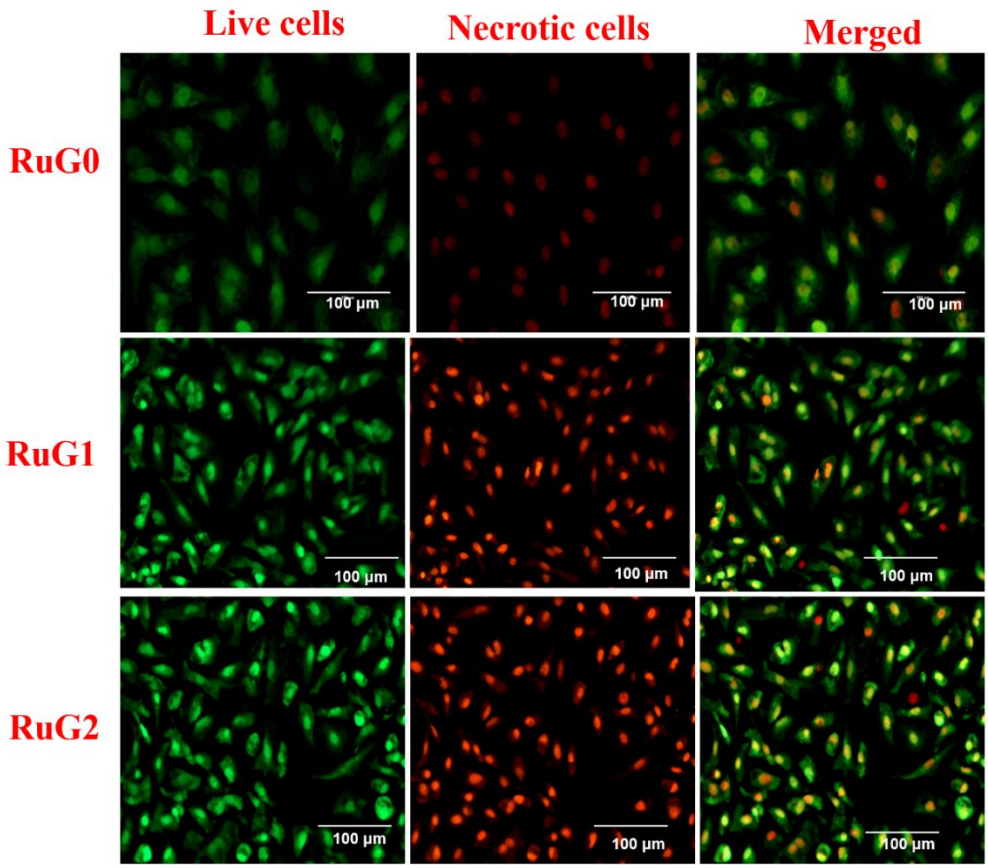

Figure S16. Apoptotic Cell Death Mechanism by the Acridine Orange−Ethidium Bromide (AO−EB) Staining Assay by coordination entities at the IC_{50} in A549 cells for 24 h (Magnification:40x, scale bar 100 µm) a) live cells b) necrotic cells c) merged.

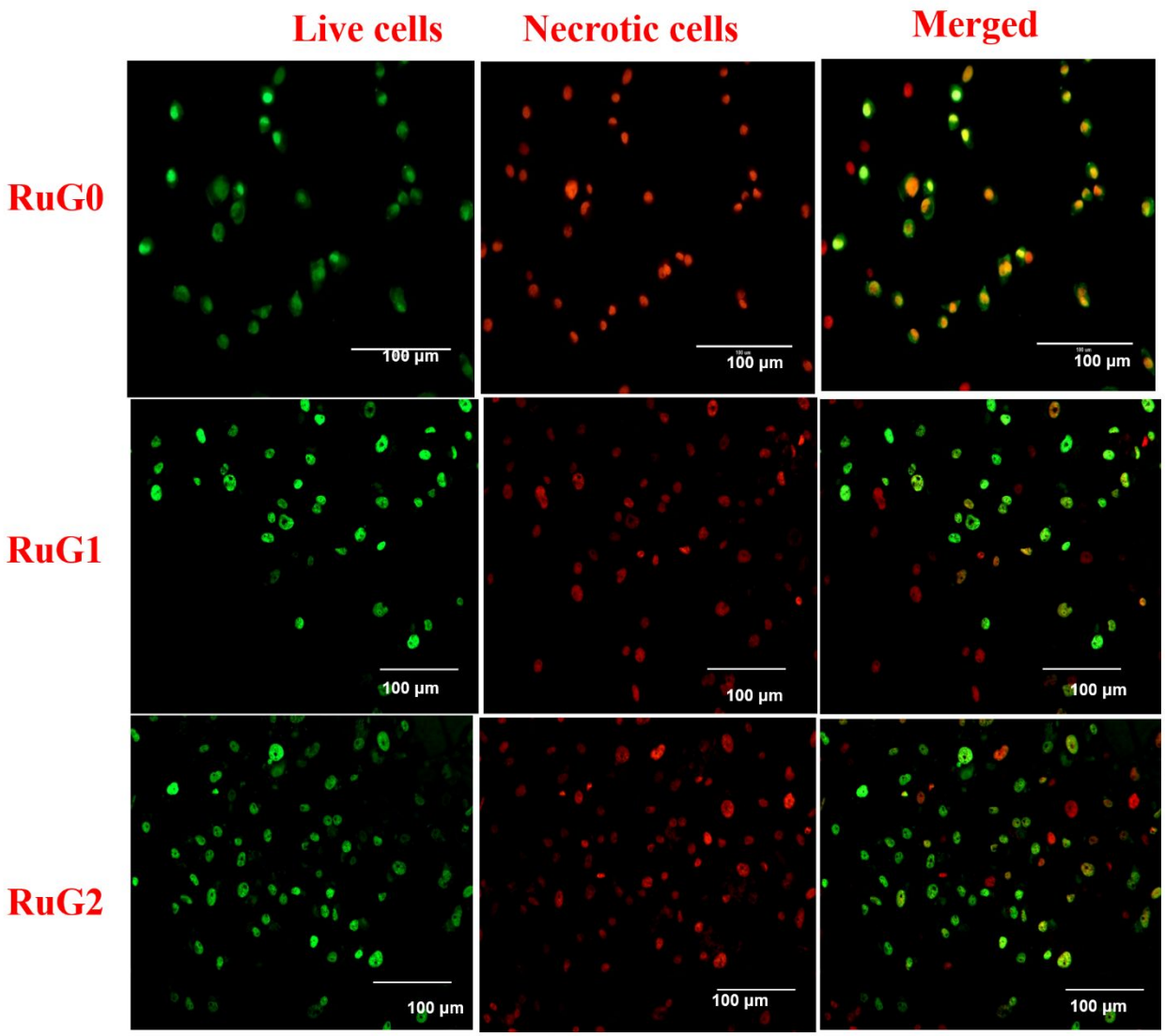

Figure S17. Apoptotic Cell Death Mechanism by the Acridine Orange−Ethidium Bromide (AO−EB) Staining Assay by coordination entities at the IC_{50} in MDA MB 231 cells for 24 h (Magnification:40x, scale bar 100 µm) a) live cells b) necrotic cells c) merged.

3.2. Nuclear morphology analysis by DAPI staining

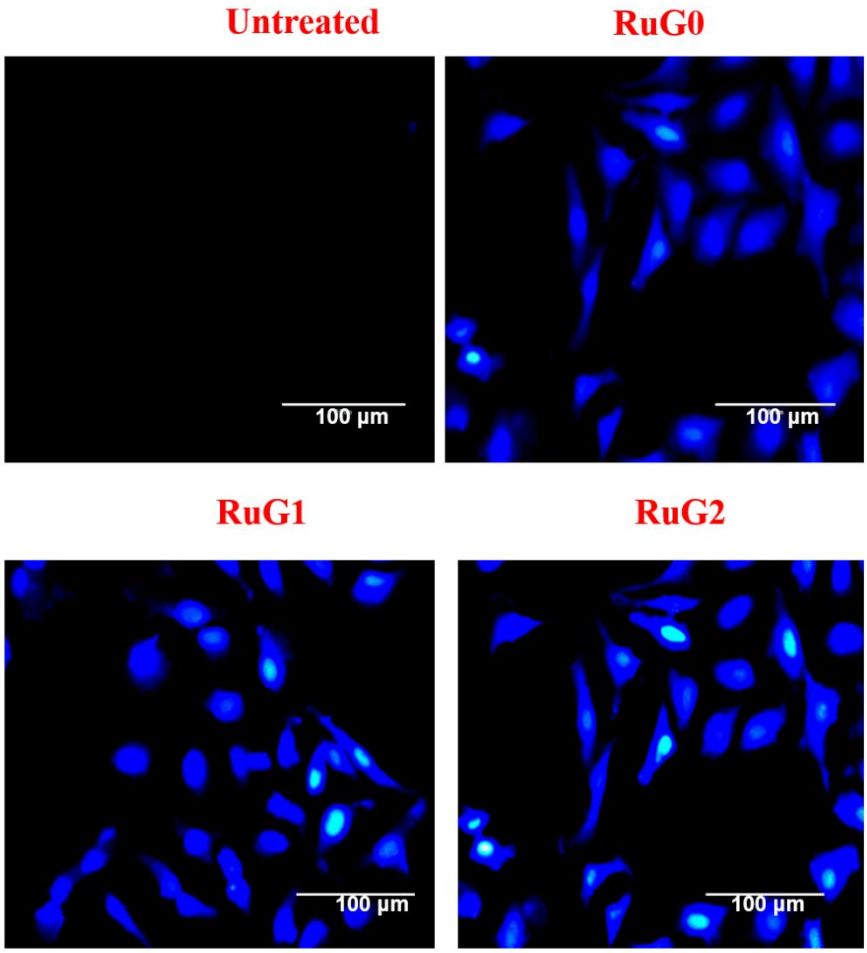

Figure S18. Nuclear morphology analysis by DAPI staining assay on A549 cells by coordination entities at the IC_{50} (Magnification: 40x, scale bar: 100 µm).

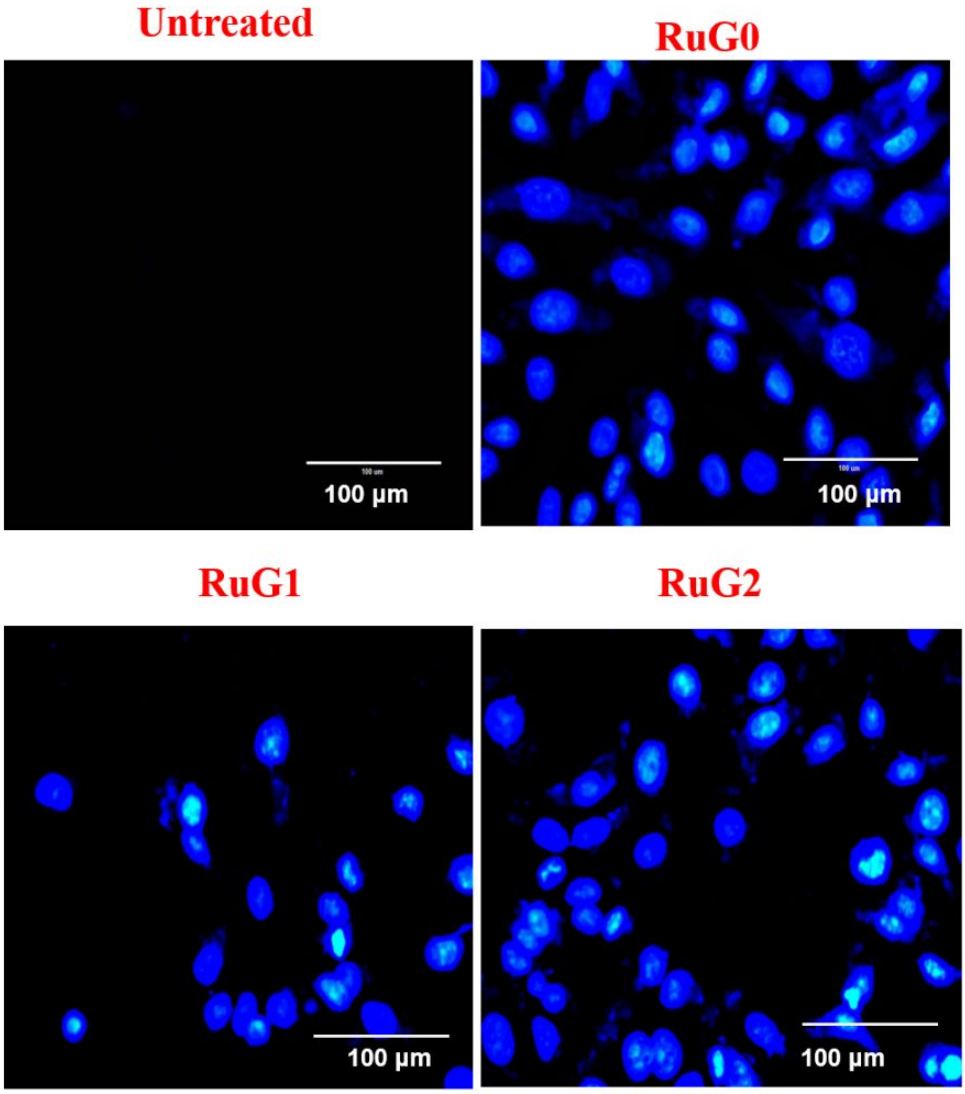

Figure S19. Nuclear morphology analysis by DAPI staining assay on MDA MB 231 cells by coordination entities at the IC_{50} (Magnification: 40x, scale bar: 100 µm).

3.3. Cell death analysis by propidium iodide- PI staining

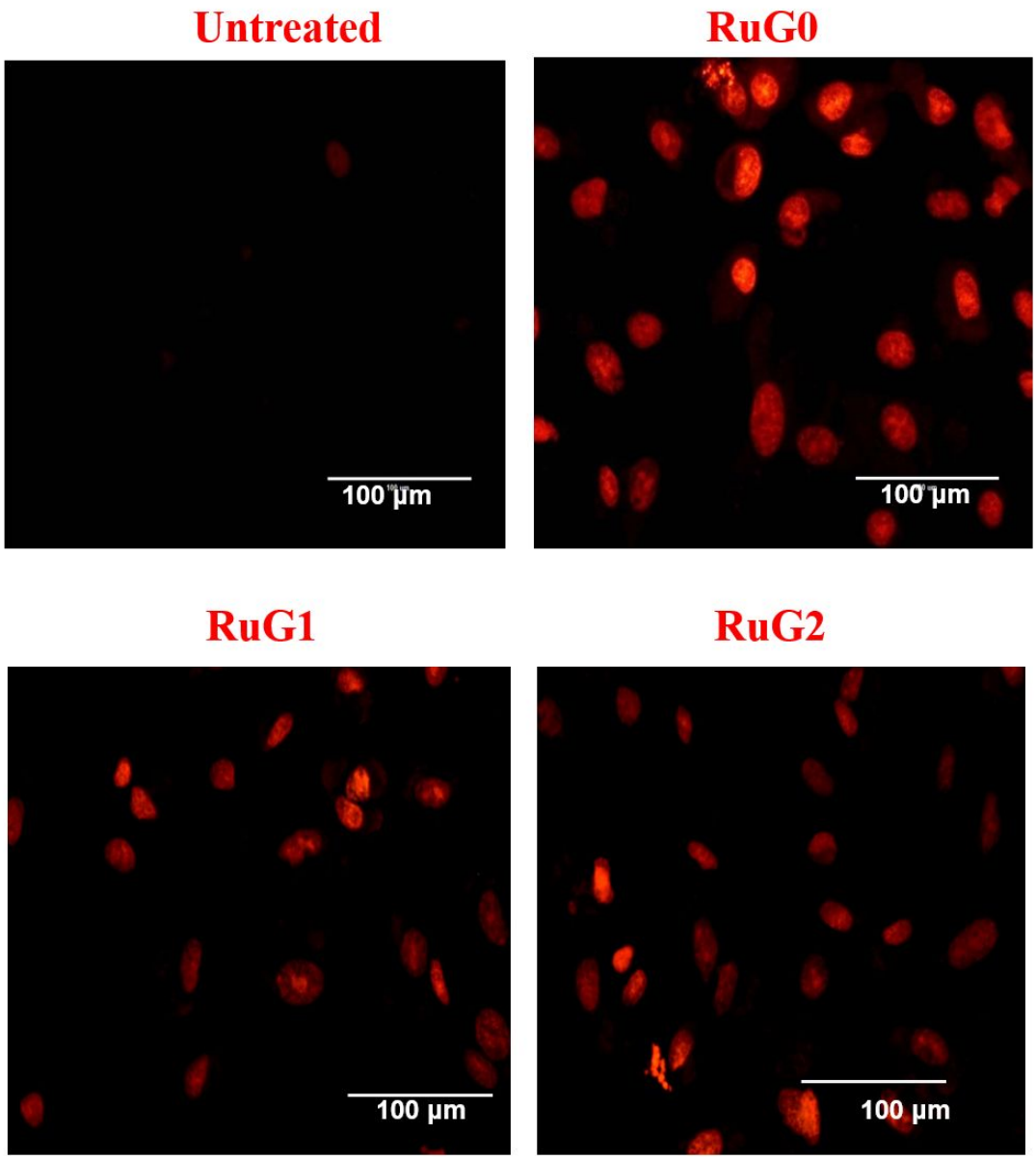

Figure S20. Cell death analysis by propidium iodide- PI staining assay on A549 cells by coordination entities at the IC_{50} concentration (Magnification: 40x, scale bar: 100 µm).

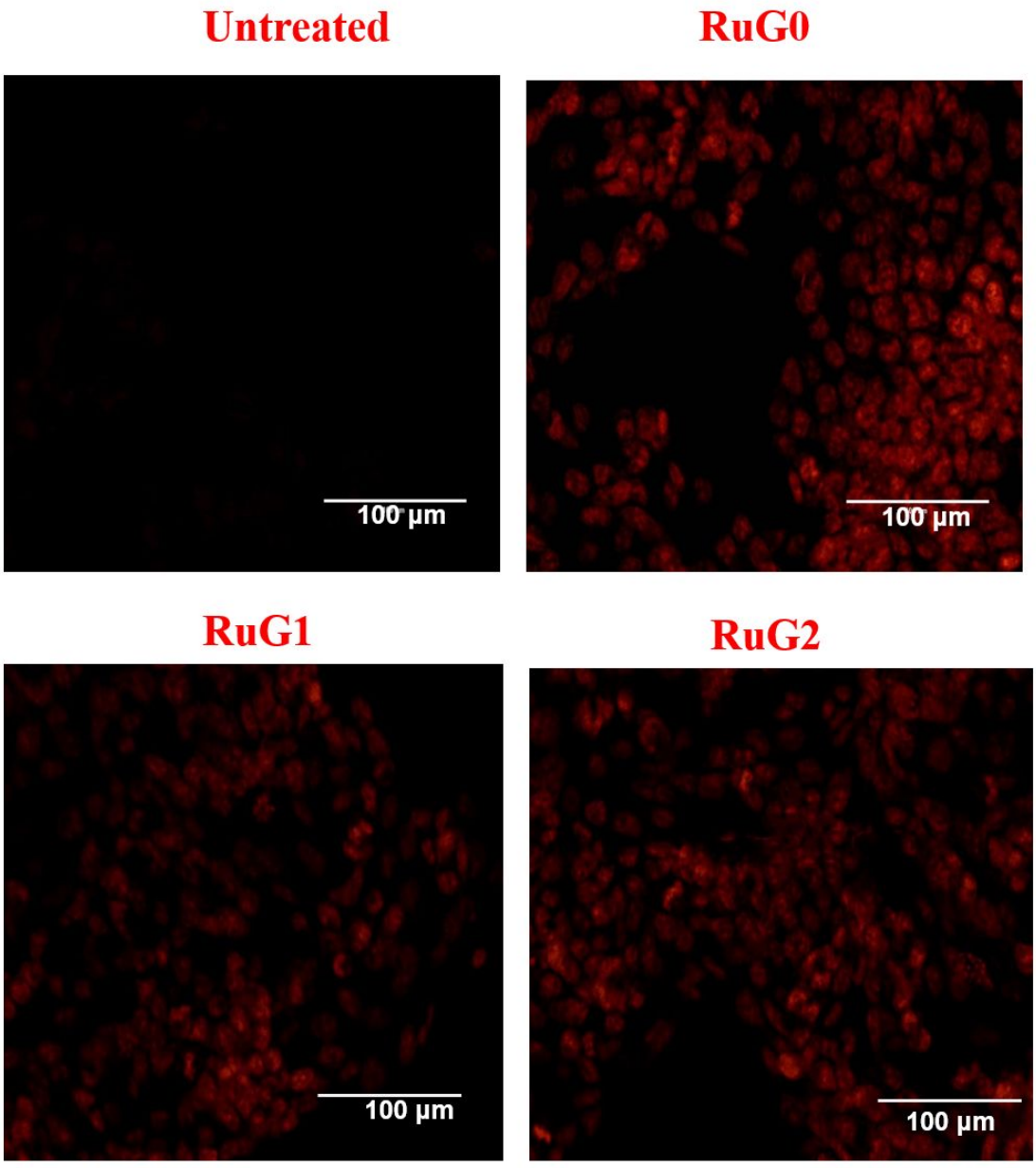

Figure S21. Cell death analysis by propidium iodide- PI staining assay on HepG2 by coordination entities at the IC_{50} concentration (Magnification: 40x, scale bar: 100 µm).

3.4. Assessment of mitochondrial membrane potential (Δψm)

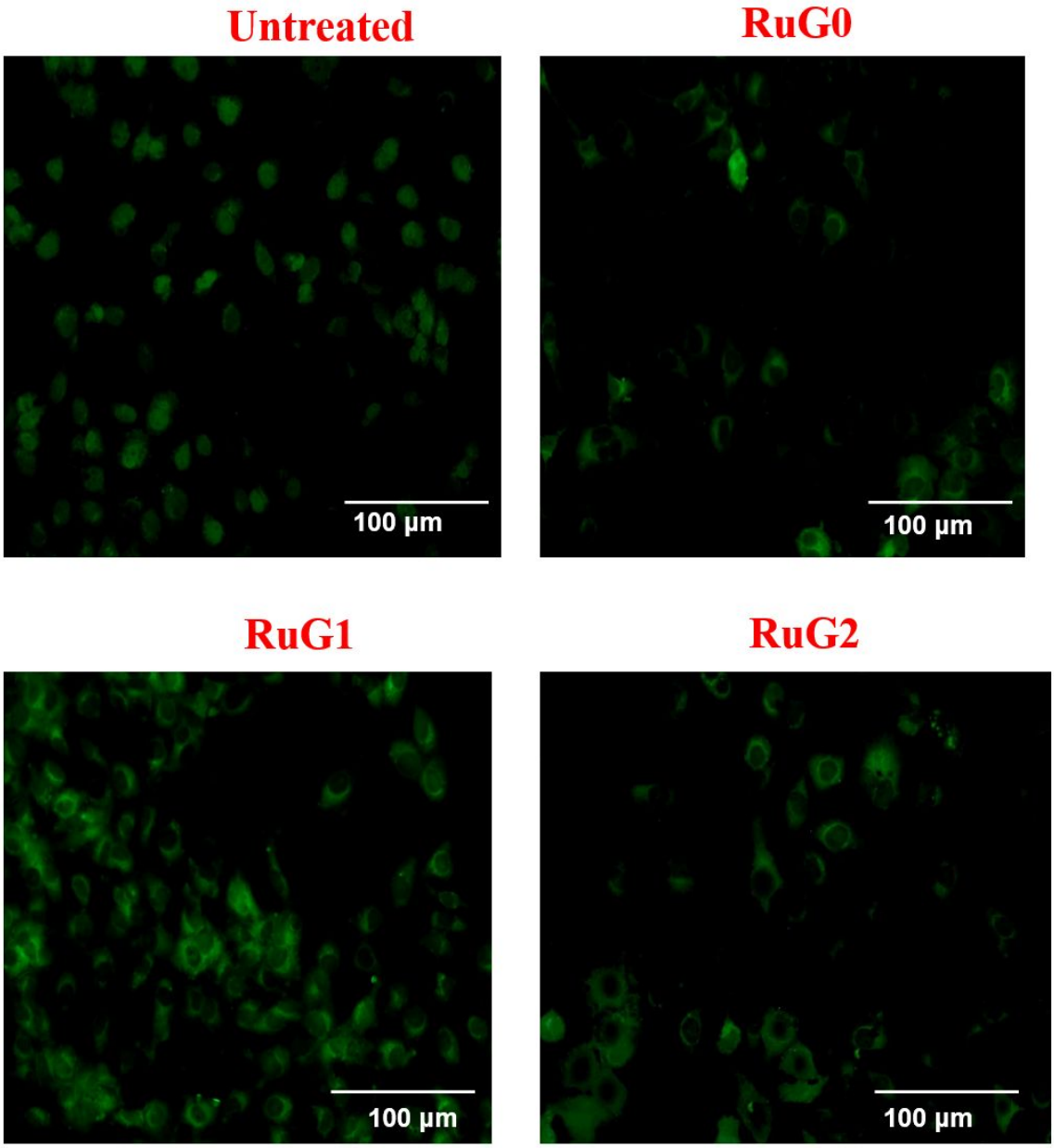

Figure S22. Rhodamine 123 staining of A549 cells with coordination entities at the IC_{50} concentration (Magnification: 40x, scale bar: 100 µm).

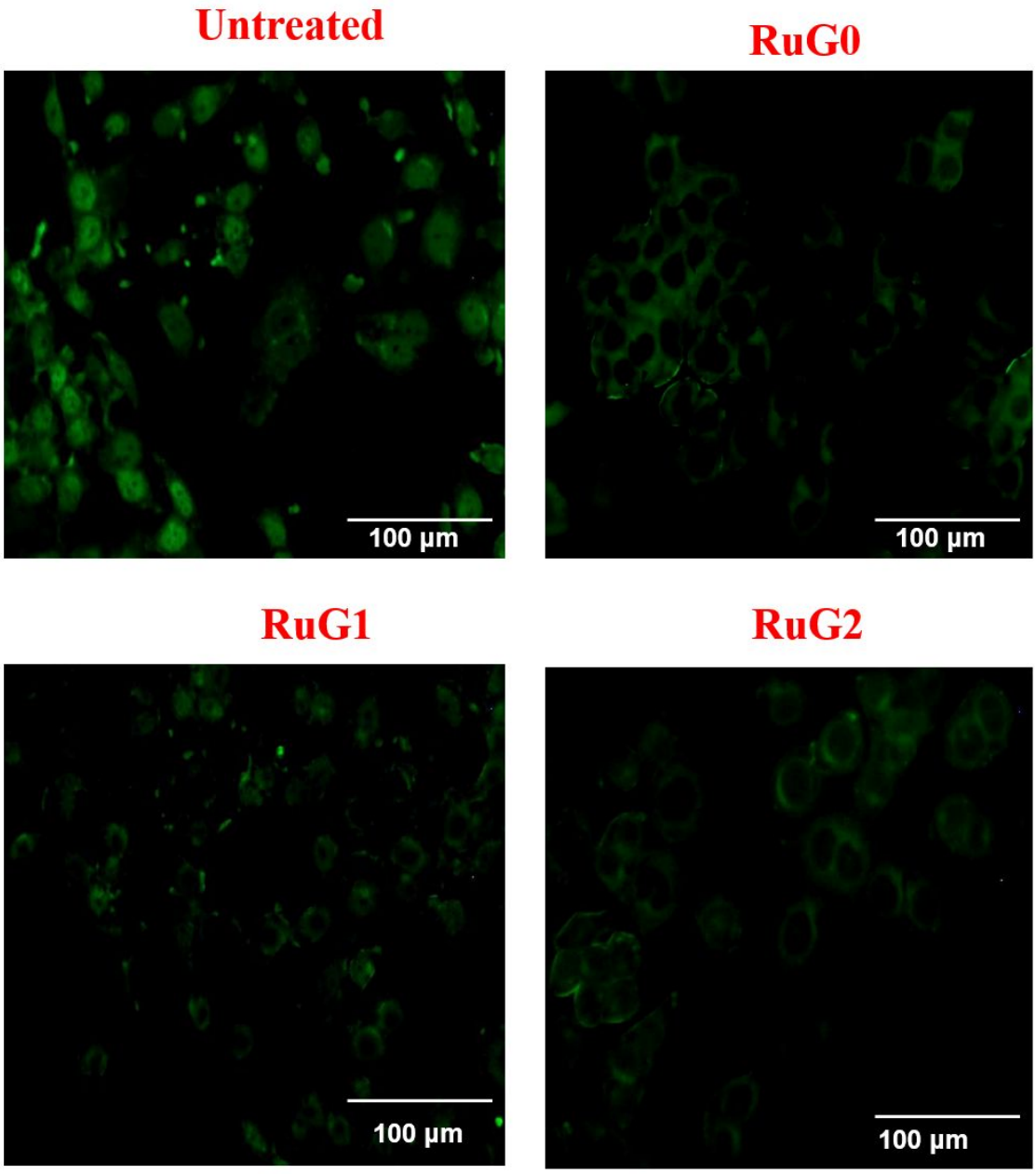

Figure S23. Rhodamine 123 staining of MDA MB 231 with coordination entities at the IC_{50} concentration (Magnification: 40x, scale bar: 100 µm).

3.5. Reactive Oxygen Species (ROS) Assay

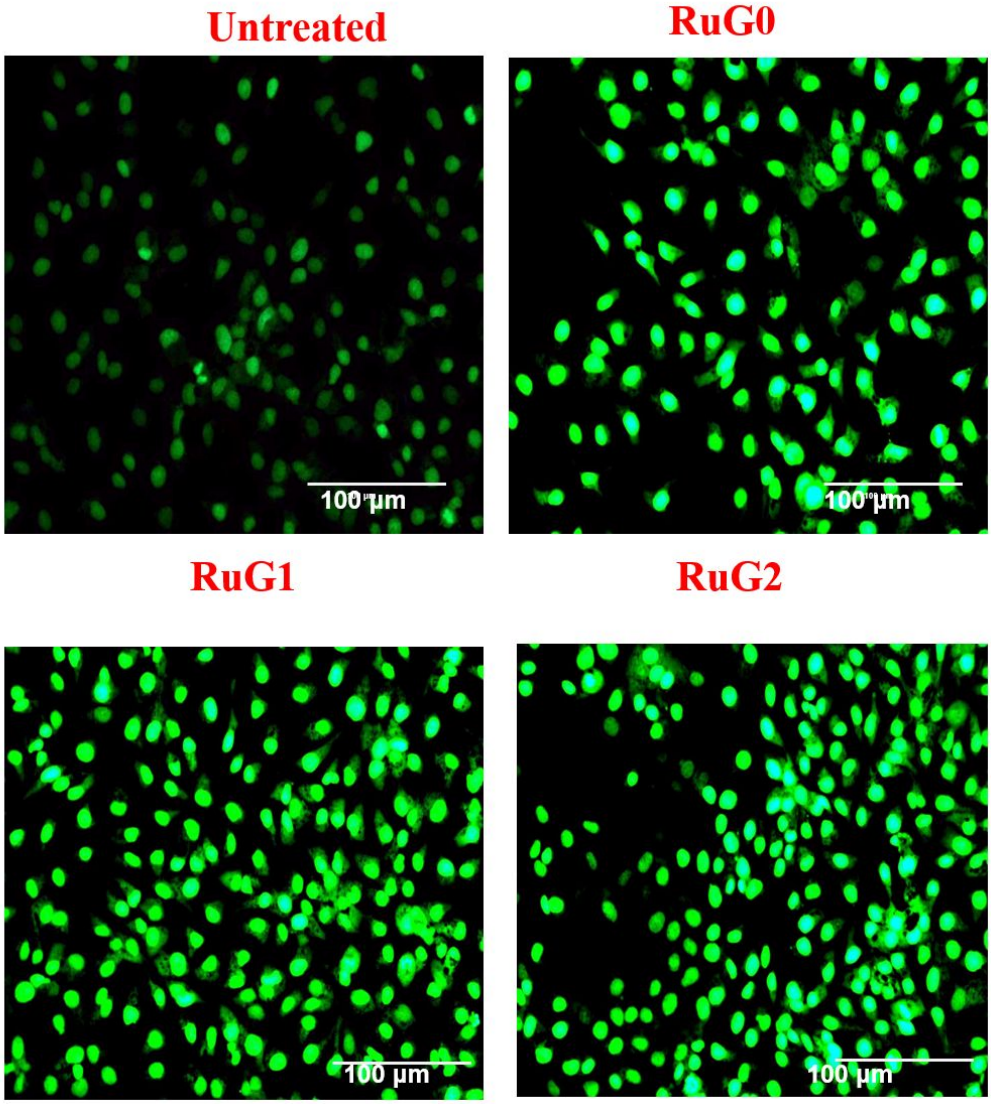

Figure S24. ROS detection on A549 cells by coordination entities at the IC_{50} concentration (Magnification: 40x, scale bar: 100 µm).

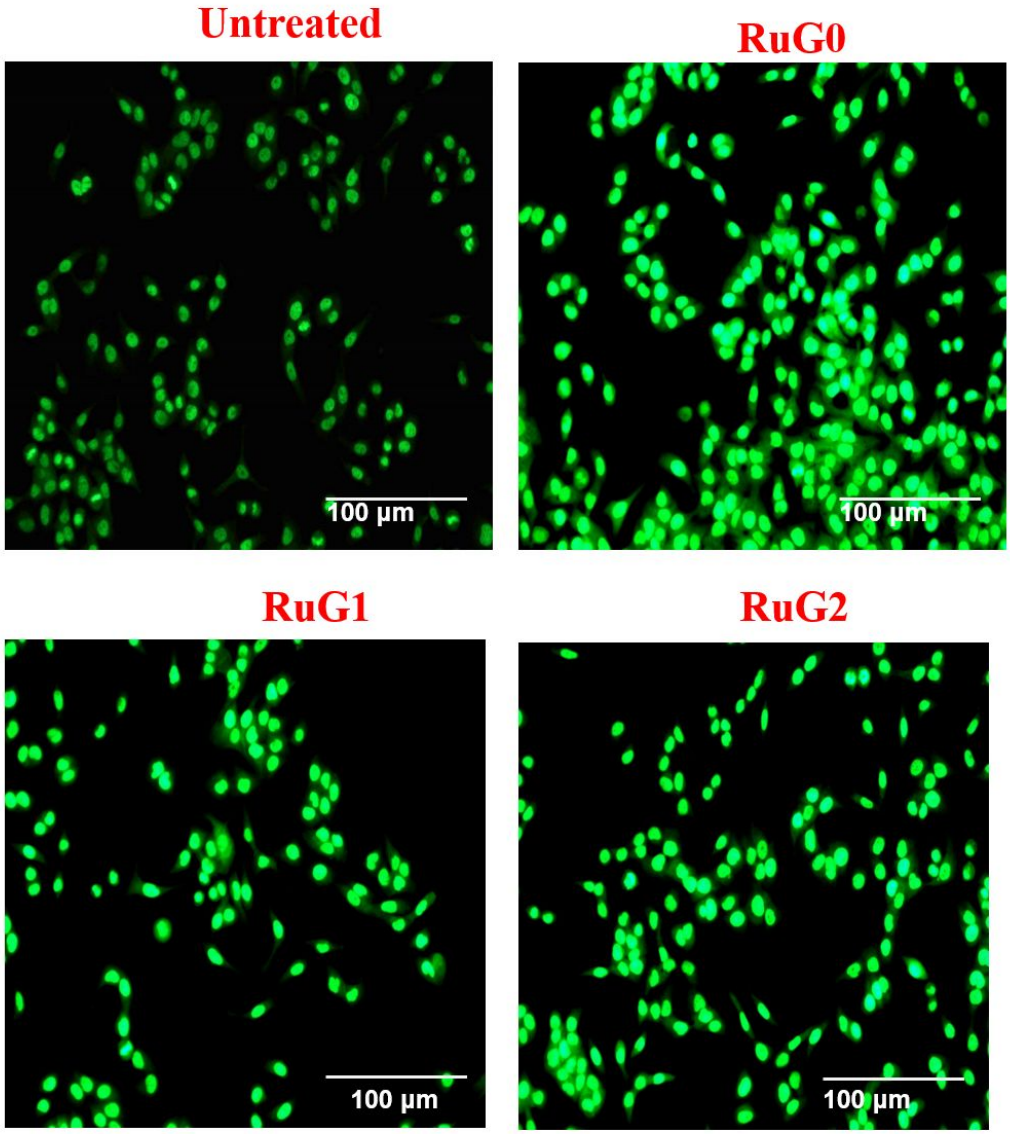

Figure S25. ROS detection on MDA MB 231 cells by coordination entities at the IC_{50} concentration (Magnification: 40x, scale bar: 100 µm).

References

(1) BIOVIA, Dassault Systèmes, BIOVIA Materials Studio. Dassault Systèmes: San Diego, 2022.
(2) Mayo, S. L.; Olafson, B. D.; Goddard, W. A. DREIDING: A Generic Force Field for Molecular Simulations. *J. Phys. Chem.* **1990**, *94* (26), 8897–8909. https://doi.org/10.1021/j100389a010.
(3) Lard, M.; Kim, S. H.; Lin, S.; Bhattacharya, P.; Ke, P. C.; Lamm, M. H. Fluorescence Resonance Energy Transfer between Phenanthrene and PAMAM Dendrimers. *Phys. Chem. Chem. Phys.* **2010**, *12* (32), 9285. https://doi.org/10.1039/b924522g.
(4) Ongari, D.; Boyd, P. G.; Kadioglu, O.; Mace, A. K.; Keskin, S.; Smit, B. Evaluating Charge Equilibration Methods To Generate Electrostatic Fields in Nanoporous Materials.

J. Chem. Theory Comput. **2019**, *15* (1), 382–401. https://doi.org/10.1021/acs.jctc.8b00669.
(5) Rappe, A. K.; Goddard, W. A. Charge Equilibration for Molecular Dynamics Simulations. *J. Phys. Chem.* **1991**, *95* (8), 3358–3363. https://doi.org/10.1021/j100161a070.
(6) Jorgensen, W. L.; Chandrasekhar, J.; Madura, J. D.; Impey, R. W.; Klein, M. L. Comparison of Simple Potential Functions for Simulating Liquid Water. *J. Chem. Phys.* **1983**, *79* (2), 926–935. https://doi.org/10.1063/1.445869.
(7) Martínez, L.; Andrade, R.; Birgin, E. G.; Martínez, J. M. PACKMOL: A Package for Building Initial Configurations for Molecular Dynamics Simulations. *J. Comput. Chem.* **2009**, *30* (13), 2157–2164. https://doi.org/10.1002/jcc.21224.
(8) Martínez, J. M.; Martínez, L. Packing Optimization for Automated Generation of Complex System's Initial Configurations for Molecular Dynamics and Docking. *J. Comput. Chem.* **2003**, *24* (7), 819–825. https://doi.org/10.1002/jcc.10216.
(9) Jewett, A. I.; Stelter, D.; Lambert, J.; Saladi, S. M.; Roscioni, O. M.; Ricci, M.; Autin, L.; Maritan, M.; Bashusqeh, S. M.; Keyes, T.; Dame, R. T.; Shea, J.-E.; Jensen, G. J.; Goodsell, D. S. Moltemplate: A Tool for Coarse-Grained Modeling of Complex Biological Matter and Soft Condensed Matter Physics. *J. Mol. Biol.* **2021**, *433* (11), 166841. https://doi.org/10.1016/j.jmb.2021.166841.
(10) Evans, D. J.; Holian, B. L. The Nose–Hoover Thermostat. *J. Chem. Phys.* **1985**, *83* (8), 4069–4074. https://doi.org/10.1063/1.449071.
(11) Maiti, P. K.; Çağın, T.; Wang, G.; Goddard, W. A. Structure of PAMAM Dendrimers: Generations 1 through 11. *Macromolecules* **2004**, *37* (16), 6236–6254. https://doi.org/10.1021/ma035629b.
(12) Kavukcu, S. B.; Şahin, O.; Seda Vatansever, H.; Kurt, F. O.; Korkmaz, M.; Kendirci, R.; Pelit, L.; Türkmen, H. Synthesis and Cytotoxic Activities of Organometallic Ru(II) Diamine Complexes. *Bioorganic Chem.* **2020**, *99*, 103793. https://doi.org/10.1016/j.bioorg.2020.103793.
(13) Ribeiro, G. H.; Costa, A. R.; de Souza, A. R.; da Silva, F. V.; Martins, F. T.; Plutin, A. M.; Batista, A. A. An Overview on the Anticancer Activity of Ru(II)/Acylthiourea Complexes. *Coord. Chem. Rev.* **2023**, *488*, 215161. https://doi.org/10.1016/j.ccr.2023.215161.
(14) Ghosh, S. Cisplatin: The First Metal Based Anticancer Drug. *Bioorganic Chem.* **2019**, *88*, 102925. https://doi.org/10.1016/j.bioorg.2019.102925.
(15) Arunachalam, A.; Rengan, R.; Umapathy, D.; Arockiam, A. J. V. Impact of Biphenyl Benzhydrazone-Incorporated Arene Ru(II) Complexes on Cytotoxicity and the Cancer Cell Death Mechanism. *Organometallics* **2022**, *41* (17), 2474–2486. https://doi.org/10.1021/acs.organomet.2c00290.
(16) Li, J.; Ma, Y.; Chen, Y.; Cai, M.; Wu, Z.; Xiong, Y.-S.; Duan, X.; Liao, X.; Wang, J. Multi-Target Antibacterial Mechanism of Ruthenium Polypyridine Complexes with Anthraquinone Groups against Staphylococcus Aureus. *RSC Med. Chem.* **2023**, *14*, 700–709. https://doi.org/10.1039/D2MD00430E.
(17) Kowsalya, E.; MosaChristas, K.; Jaquline, C. R. I.; Balashanmugam, P.; Devasena, T. Gold Nanoparticles Induced Apoptosis via Oxidative Stress and Mitochondrial Dysfunctions in MCF-7 Breast Cancer Cells. *Appl. Organomet. Chem.* **2021**, *35* (1), e6071. https://doi.org/10.1002/aoc.6071.
(18) Liu, J.; Wu, Y.; Yang, G.; Liu, Z.; Liu, X. Mitochondrial Targeting Half-Sandwich Iridium(III) and Ruthenium(II) Dppf Complexes and in Vitro Anticancer Assay. *J. Inorg. Biochem.* **2023**, *239*, 112069. https://doi.org/10.1016/j.jinorgbio.2022.112069.

(19) Angelé-Martínez, C.; Nguyen, K. V. T.; Ameer, F. S.; Anker, J. N.; Brumaghim, J. L. Reactive Oxygen Species Generation by Copper(II) Oxide Nanoparticles Determined by DNA Damage Assays and EPR Spectroscopy. *Nanotoxicology* **2017**, *11* (2), 278–288. https://doi.org/10.1080/17435390.2017.1293750.
(20) Prabaharan, R.; Rengan, R.; Umapathy, D.; Arockiam, A. J. V.; Małecki, J. G. Assessment of Antiproliferative Activity of New Half-Sandwich Arene Ru (II) Furylbenzhydrazone Complexes. *Appl. Organomet. Chem.* **2022**, *36* (2), e6512. https://doi.org/10.1002/aoc.6512.
(21) Mandal, S.; Tarai, S. K.; Patra, P.; Nandi, P.; Sing, S.; Rajak, B.; Moi, S. C. Brief Research on the Biophysical Study and Anticancer Behavior of Pt(II) Complexes: Their DNA/BSA Binding, Molecular Docking, and Cytotoxic Property. *Langmuir* **2022**, *38* (44), 13613–13625. https://doi.org/10.1021/acs.langmuir.2c02490.
(22) Morris, G. M.; Huey, R.; Lindstrom, W.; Sanner, M. F.; Belew, R. K.; Goodsell, D. S.; Olson, A. J. AutoDock4 and AutoDockTools4: Automated Docking with Selective Receptor Flexibility. *J. Comput. Chem.* **2009**, *30* (16), 2785–2791. https://doi.org/10.1002/jcc.21256.
(23) Schrödinger Release 2022-2: Maestro, Schrödinger, LLC, New York, NY, 2022.